Int J Thermophys (2018) 39:88
https://doi.org/10.1007/s10765-018-2409-9

Lattice Boltzmann Simulations for Melting and Resolidification of Ultrashort Laser Interaction with Thin Gold Film

Ling Li[1] · **Mingyang Wu**[1] · **Ling Zhou**[1]

Received: 12 September 2017 / Accepted: 30 May 2018

Abstract The interaction between the laser and material is commonly described by the macroscale method, two-temperature model (TTM), and the microscale method, molecular dynamics. In the present paper, the melting and resolidification of ultrashort laser interaction with thin gold film is investigated in terms of a meso-scale method. The lattice Boltzmann method (LBM) including the electron–phonon collision term is established. A fixed grid approach is applied in the phonon subsystem to describe the phase change. The transition zone between solid and liquid is treated as the porous medium. The results predicted by the LBM coincide with the experiment data quite well. In addition, the detailed comparisons between the TTM with interfacial tracking method and the LBM are conducted. The influences of the laser fluences and pulse widths on the transition phase are also investigated.

Keywords Lattice Boltzmann simulation · Phase change · Ultrashort laser radiation

List of symbols

a	Thermal diffusion coefficient ($m^2 \cdot s^{-1}$)
C	Heat capacity ($J \cdot m^{-3} \cdot K^{-1}$)
F	External force (N)
F_l	Liquid fraction
G	Electron–lattice coupling factor ($W \cdot m^{-3} \cdot K^{-1}$)
h_m	Latent heat of melting ($J \cdot kg^{-1}$)
J	Heat source fluence of laser ($J \cdot m^{-2}$)

✉ Ling Li
liling@usst.edu.cn

[1] School of Energy and Power Engineering, University of Shanghai for Science and Technology, Shanghai 200093, China

Published online: 07 June 2018

k	Electron wave vector (m^{-1})
k_B	Boltzmann constant ($J \cdot K^{-1}$)
L	Thickness of gold film (m)
$M_{k,k'}$	Electron–phonon matrix element
m	Mass (kg)
N	Number density of atom (m^{-3})
q	Phonon wave vector (m^{-1})
R	Reflectivity of gold film
R_g	Gas constant for gold ($J \cdot kg^{-1} \cdot K^{-1}$)
S	Heat source of unit volume ($W \cdot m^{-3}$)
s	Interfacial location (m)
T	Temperature (K)
$T_{l,I}$	Interfacial temperature for lattices (K)
t	Time (s)
t_p	Full width at half maximum (FWHM) pulse width (s)
U	Potential energy coefficient
V	Phase space
v	Velocity ($m \cdot s^{-1}$)
w	Weighting factor
x	Coordinate (m)

Greek symbols

δ	Optical penetration depth (m)
δ_b	Ballistic range (m)
Δl	Length of the transition zone (m)
ε	Energy (J)
λ	Thermal conductivity ($W \cdot m^{-1} \cdot K^{-1}$)
$\hbar$	Planck constant (J·s)
ξ	Radius of phase transition zone (K)
ρ	Density ($kg \cdot m^{-3}$)
Γ	Relaxation time for the collision between different particles (s)
τ	Relaxation time for the collision in the homogeneous particles (s)
ω	Frequency (s^{-1})
Ω	Collision term

Subscripts

D	Debye
e	Electron
eq	Thermal equilibrium state
F	Fermi
i	Initial
I	Interfacial
l	Lattice

ph Phonon
s Sound

1 Introduction

The embryonic development of ultrafast science stems from advances made in the generation of ultrashort laser pulses. Beginning with mode-locking of glass lasers in the 1960s, the development of dye laser brought the pulse width down from picoseconds to femtoseconds [1]. As concepts and methodologies have evolved over the past two decades, the ultrafast laser has been used in various applications such as the laser sintering [2, 3], ablation [4] and hole drilling [5].

The simulation of the laser–material interaction can be divided into two main approaches. The first one is the macroscopic (or continuum) approach which is derived from the phenomenological energy conversation of the continuum medium. The two-temperature model (TTM), which is widely used in ultrashort laser heating, is an exact example. The first TTM is pioneered by Anisimov et al. [6]. This model, however, is not based on a rigorous derivation. Qiu and Tien [7] succeeded in deriving the TTM rigorously from the Boltzmann equation and gave physical meaning to it. To date, numerous TTMs have been proposed to describe the nonequilibrium energy transport of the free electrons and lattices during the short-pulse laser interaction with materials. And they were also developed by adding the relaxation effect [8, 9] and the electron drifting effect [10]. Generally, the electron temperature and lattice temperature below the melting point predicted by the TTM can coincide with the experimental data quite well [8, 10].

For the practical laser–material processing, such as sintering or ablation, the phase changes are of importance. Two-temperature model, which is derived from the continuum energy equation of both electrons and lattices, should apply an obvious interface to catch the phase change behavior [11]. The melting [11–15] and vaporization [4, 16–19] of gold films subject to nano- to femtosecond laser pulses were investigated using the TTM in conjunction with the interfacial tracking method. Our previous work also applied the interfacial tracking method to a hyperbolic TTM to investigate the effect of the electron relaxation [20]. However, the interfacial tracking method leads to a bizarre mutation of the temperature at the interface (which can also be seen in the following content) and cannot describe the transition phase between solid and liquid [18]. In addition, TTM with the interfacial tracking method still cannot be applied to the deformation of the irradiated target, e.g., the growth of the ablation plume and the formation of the ablation hole [21].

On the other extreme, the medium can be considered made of small particles (atom or molecule) and these particles collide with each other. This method is the microscopic approach or molecular dynamics method (MDM). MDM can describe the melting and ablation behavior more precisely. Yang et al. [22] investigated the neck growth in the laser sintering (melting) process of the nanoparticles using MDM. Upadhyay and Urbassek [5] studied, with the help of MDM, the material processes occurring for fixed laser fluence in a thin metal film induced by ultrafast laser irradiation. Ji and Zhang [23] used the ab initio MDM to study the femtosecond laser processing of

germanium. However, MDM is based on electron–lattice thermal equilibrium [21]. During the ultrafast laser interaction with the material, the nonequilibrium of the electrons and lattices cannot be described by MDM. Yamashita et al. [21] developed a combined method of TTM and MDM, which can handle the electron–lattice coupling issue theoretically, while there still remains some differences between their simulation results and the experimental data. Furthermore, the MDM is quite time-consuming.

The lattice Boltzmann method (LBM) is a meso-scale method sitting at the middle of both mentioned techniques. The main idea of Boltzmann is to bridge the gap between microscale and macroscale by not considering each particle behavior alone but the behavior of a collection of particles as a unit [24]. The lattice Boltzmann method has emerged to offer huge potentials for solving the morphological evolution of topographically complicated phase boundaries during separation of phases [25, 26], melting/solidification processes [27–32] and laser cutting problem [33]. Also, LBM is quite inherently parallelizable and time-efficient [30, 31].

However, in the most existing work on LBM, the rate of change between the final and initial distribution function only results from the homogeneous-particle collision, which leads to the classical Fourier law [7, 24], but neglect the collision between electrons and phonons (the vibration of the lattice). The latter is quite important for the ultrashort laser interaction with the material, since the electron–phonon scattering is the main reason resulting in the nonequilibrium of the electrons and lattices. In present paper, we use the LBM to solve the melting and resolidification of a thin gold film irradiated by the ultrashort pulsed laser. The scattering term between the electron and lattice is considered. A fixed grid approach is applied to describe the phase change, and the transition zone between solid and liquid is treated as the porous medium. In addition, the detailed comparisons between the TTM with interfacial tracking method and the LBM are conducted. The influences of the laser fluences and pulse widths on the transition phase are also investigated.

2 Physical Model

In this section, we firstly review the phenomenological model—the TTM. And then, the model of LBM is proposed and the detailed numerical solution is also presented. Figure 1 shows the schematic of the problem under consideration. Figure 1a shows a metal film with a thickness of L and an initial temperature of T_{i} subjected to a temporal Gaussian laser pulse with a full width at half maximum (FWHM) pulse width of t_p and a fluence of J ($\mathrm{J{\cdot}m^{-2}}$) from the right-hand surface ($x = L$). The pulse width is illustrated in Fig. 1b.

2.1 Two-Temperature Model with the Interfacial Tracking Method

Energy deposits into materials in different ways, depending on the nature of heating methods and the structure of materials [7]. It can deposit simultaneously on all energy carriers through contact heating at surfaces, e.g., electrons and phonons, or selectively on a particular group of carriers by radiation heating. Radiation heating firstly excites free/bound electrons in metals, and then, the energy in the electrons transfers into

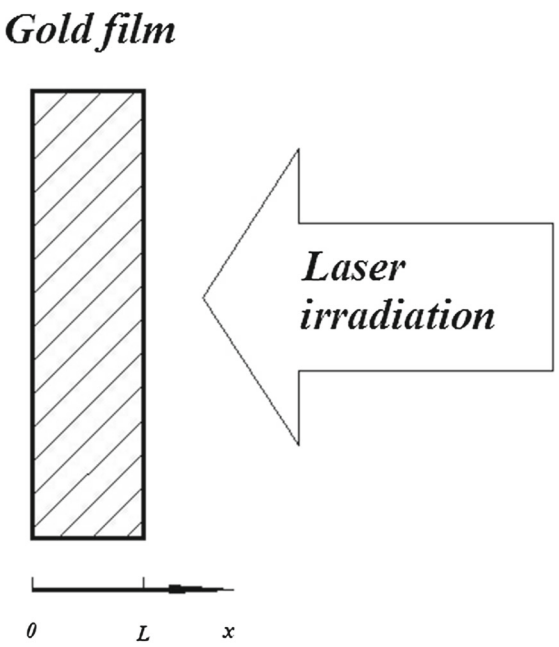

(a) Thin gold film irradiated by pulsed laser

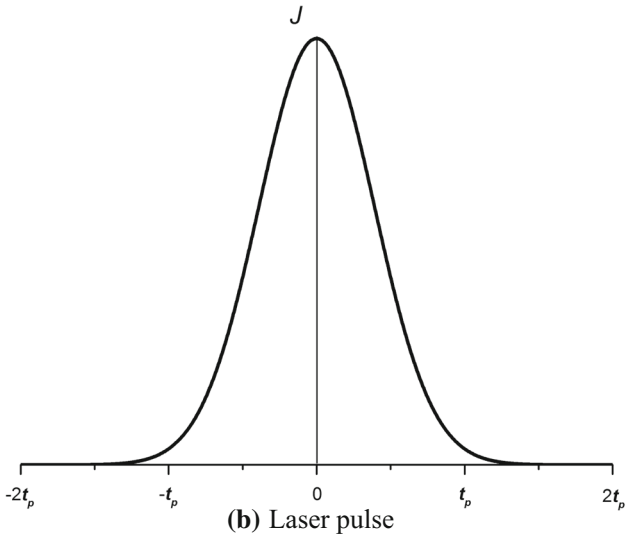

(b) Laser pulse

Fig. 1 Physical model

the phonons. The mechanism of heating becomes important when the time scale of interest is comparable with the characteristic time for different energy carriers to communicate with each other. For the ultrafast laser interaction with the material, the

energy transport by each group of carriers and the interactions among them need to be considered [34].

In Fig. 1a, the laser–material interaction can be approximated to be one-dimensional, when the radius of laser beam is much larger than the thickness of the film [16]. The nonequilium of the electron and lattice can be described by TTM as follows [6]

$$C_{\mathrm{e}}\frac{\partial T_{\mathrm{e}}}{\partial t}=\frac{\partial}{\partial x}\left(\lambda_{\mathrm{e}}\frac{\partial T_{\mathrm{e}}}{\partial x}\right)-G(T_{\mathrm{e}}-T_{\mathrm{l}})+S \tag{1}$$

$$C_{\mathrm{l}}\frac{\partial T_{\mathrm{l}}}{\partial t}=\frac{\partial}{\partial x}\left(\lambda_{\mathrm{l}}\frac{\partial T_{\mathrm{l}}}{\partial x}\right)+G(T_{\mathrm{e}}-T_{\mathrm{l}}) \tag{2}$$

where T represents the temperature, t is the time, x is the coordinate, C is the heat capacity, λ is the thermal conductivity, and G is the coupling factor. The subscripts, e and l, are referred to as the electron and lattice, respectively. The laser irradiation is treated as the source term S.

The source term S in Eq. 1 can be described by the following equation [10]

$$S=0.94\frac{1-R}{t_p(\delta+\delta_b)[1-e^{-L/(\delta+\delta_b)}]}J\exp\left[-\frac{L-x}{\delta+\delta_b}-2.77\left(\frac{t}{t_p}\right)^2\right] \tag{3}$$

where R is the reflectivity of the film and t is the time which begins from $-2t_p$, see Fig. 1b. δ and δ_b are the optical penetration depth and the electron ballistic range, respectively. $1-e^{-L/(\delta+\delta_b)}$ is to correct the finite film thickness effect.

Since the TTM has to apply an obvious interface to catch the melting and resolidification behavior, an extra equation should be added to calculate the interface velocity. The interfacial velocity v_{I} of the ultrafast phase change process depends on the nucleation dynamics [14], i.e.,

$$v_{\mathrm{I}}=v_0\left[1-\exp\left(-\frac{h_{\mathrm{m}}}{R_{\mathrm{g}}T_{\mathrm{m}}}\frac{T_{\mathrm{l,I}}-T_{\mathrm{m}}}{T_{\mathrm{l,I}}}\right)\right] \tag{4}$$

where v_0 is the maximum interface velocity, h_{m} is the latent heat of melting, R_{g} is the gas constant, $T_{\mathrm{l,I}}$ is the interfacial temperature, and T_{m} is the melting temperature of the film.

More numerical details of the interfacial tracking method can be found in Refs. [13, 14]. Our previous work also investigates the melting and resolidification of gold film irradiated by laser pulses less than 100 fs [20].

2.2 Boltzmann Transport Model for the Electron–Phonon Interaction

Qiu and Tien [7] proposed the TTM under the quasi-classical particle framework by the Boltzmann transport equation. Chen et al. [10] also developed the TTM by including the three equations of the conservation of number density, momentum and energy for the electron system based on the Boltzmann transport equation. However, Refs [7, 10]

mainly focus on the electron system but neglect the heat conduction of lattice which is significant, especially for the phase change issue [13].

In present paper, we propose a two-step lattice Boltzmann model which includes both the electron subsystem and the phonon subsystem (vibrations of the lattice). The distribution functions for electrons and phonons are assumed as f_{e} and f_{ph}. According to the Boltzmann transport equation, the electron and lattice subsystem can be described as

$$\frac{\mathrm{d}f_{\mathrm{e}}}{\mathrm{d}t} = \frac{\partial f_{\mathrm{e}}}{\partial t} + v_{\mathrm{e}} \cdot \nabla_r f_{\mathrm{e}} + \frac{1}{\hbar} F_{\mathrm{e}} \cdot \nabla_k f_{\mathrm{e}} = \Omega_{\mathrm{e-e}} - \Omega_{\mathrm{e-ph}} + S \tag{5}$$

$$\frac{\mathrm{d}f_{\mathrm{ph}}}{\mathrm{d}t} = \frac{\partial f_{\mathrm{ph}}}{\partial t} + v_{\mathrm{ph}} \cdot \nabla_r f_{\mathrm{ph}} + \frac{1}{\hbar} F_{\mathrm{ph}} \cdot \nabla_k f_{\mathrm{ph}} = \Omega_{\mathrm{ph-ph}} + \Omega_{\mathrm{e-ph}} \tag{6}$$

where v is the speed, k is the wave vector, F is the external force, and $\hbar$ denotes Planck constant divided by 2π. $\Omega_{\mathrm{e-e}}$ and $\Omega_{\mathrm{ph-ph}}$ are the collision terms in the homogeneous particles (electrons or phonons). $\Omega_{\mathrm{e-ph}}$ represents the collision between electrons and phonons. And the linear Bhatnagar–Gross–Krook–Welander (BGKW) approximation is commonly used to calculate the collision terms in the homogeneous particles, i.e., [24]

$$\Omega_{\mathrm{e-e}} = \frac{1}{\tau_{\mathrm{e}}} \left(f_{\mathrm{e}}^{\mathrm{eq}} - f_{\mathrm{e}} \right) \tag{7}$$

$$\Omega_{\mathrm{ph-ph}} = \frac{1}{\tau_{\mathrm{ph}}} \left(f_{\mathrm{ph}}^{\mathrm{eq}} - f_{\mathrm{ph}} \right) \tag{8}$$

$\Omega_{\mathrm{e-ph}}$ causes the energy exchange between electrons and the phonons. The electron–lattice collision term $\Omega_{\mathrm{e-ph}}$ can be obtained by standard Bloch–Boltzmann–Peierls formulas [35, 36]

$$\Omega_{\mathrm{e-ph}} = -\frac{4\pi}{\hbar N} \sum_{k} |M_{kk'}|^2 \, f_{e,k}(1 - f_{e,k'})[f_{ph,q}\delta(\varepsilon_k - \varepsilon_{k'} + \hbar\omega_q) - (f_{ph,q} + 1)\delta(\varepsilon_k - \varepsilon_{k'} - \hbar\omega_q)] \tag{9}$$

where k is the electron wave vector of incidence, k' is the electron wave vector of scattering, q is the phonon wave vector of scattering which equals $q = k - k'$, $M_{kk'}$ is the electron–phonon matrix element, and ω is the frequency.

Kaganov et al. [37] assumed a Fermi–Dirac distribution for electrons and a Bose–Einstein distribution for phonons; the energy transfer rate between the electrons and the lattice was estimated by summing all one-phonon emission and absorption processes

$$\Omega_{\mathrm{e-ph}} = \frac{2}{(2\pi)^3} \frac{m_{\mathrm{e}}^2 U^2 (k_{\mathrm{B}} T_{\mathrm{D}})^5}{\hbar \rho v_{\mathrm{s}}^4} \left\{ \left(\frac{T_{\mathrm{e}}}{T_{\mathrm{D}}} \right)^5 \int_0^{T_{\mathrm{D}}/T_{\mathrm{e}}} \frac{\eta^4}{e^{\eta} - 1} \mathrm{d}\eta - \left(\frac{T_{\mathrm{l}}}{T_{\mathrm{D}}} \right)^5 \int_0^{T_{\mathrm{D}}/T_{\mathrm{l}}} \frac{\eta^4}{e^{\eta} - 1} \mathrm{d}\eta \right\} \tag{10}$$

where m_{e} is the mass of electron, U is a coefficient of the potential energy that describes the interaction between electrons and the lattice, T_{D} is the Debye temperature, ρ is

the mass density of the material, and v_s is the velocity of sound. In the limiting case of high electron temperatures T_e, $T_l >> T_D$, Eq. 10 becomes

$$\Omega_{e-ph} = \frac{\pi^2 N m_e v_s^2}{6}\left[\frac{1}{\Gamma_e(T_e)} - \frac{1}{\Gamma_e(T_l)}\right] \tag{11}$$

For the electron thermal relaxation, both electron–phonon and electron–electron scatterings contribute to the electron collision frequency. Hence, the electron relaxation time Γ_e is expressed as follows [38],

$$\Gamma_e = \frac{1}{\omega_{e-e} + \omega_{e-ph}} \tag{12}$$

where ω_{e-e} and ω_{e-ph} are the electron–electron and electron–phonon collision rates. When $T_l > T_D$ and $T_e << T_F$, $\omega_{e-e} = \omega_{e,0}\,(T_F/T_e)^2$ and $\omega_{e-ph} = \omega_{ph,0}\,(T_F/T_l)$ with ω_{e-e} and ω_{e-ph} being constants of a metal. $\Gamma_e(T_e)$ and $\Gamma_e(T_l)$ in Eq. 12 are obtained by $\Gamma_e(T_e) = \Gamma_e(T_e, T_l = T_e)$ and $\Gamma_e(T_l) = \Gamma_e(T_e = T_l, T_l)$.

2.3 Numerical Solution for LBM

In present work, a D1Q2 model defined in Ref. [24] is used. The Boltzmann transport equation (Eq. 12) with BGKW approximation and the electron–lattice scattering term can be discretized as

$$\begin{aligned} f^*_{e,i}(x, t+\Delta t) = {} & f_{e,i}(x,t) - \frac{\Delta t}{\tau_e}[f_{e,i}(x,t) - f^{eq}_{e,i}(x,t)] \\ & - \frac{w_{e,i}\Delta t}{C_e}\Omega_{e-ph} + \frac{w_{e,i}\Delta t}{C_e}S \end{aligned} \tag{13}$$

$$\begin{aligned} f^*_{ph,j}(x, t+\Delta t) = {} & f_{ph,j}(x,t) - \frac{\Delta t}{\tau_l}[f_{ph,j}(x,t) - f^{eq}_{ph,j}(x,t)] \\ & + \frac{w_{ph,j}\Delta t}{C_l}\Omega_{e-ph} - \frac{w_{ph,j}\Delta t}{C_l}\frac{\partial\,(h_m F_l)}{\partial t} \end{aligned} \tag{14}$$

where $w_{e,i}$ and $w_{ph,j}$ are the weighting factors for electrons and phonons which are 0.5 for D1Q2 model, and F_l is the liquid fraction. The superscript * denotes the distribution function obtained in the collision step, and the subscript i (or j) is 1 or 0. The last term of Eq. 14 is the latent heat when the phase change takes place. (Here we treat the latent heat as an extra source.) The distribution functions of equilibrium state $f^{eq}_{e,i}$ and $f^{eq}_{ph,j}$ are as follows:

$$f^{eq}_{e,i} = w_{e,i} T_e \tag{15}$$

$$f^{eq}_{ph,j} = w_{ph,j} T_l \tag{16}$$

The electron temperature T_e and the lattice temperature T_l can be calculated as follows:

$$T_e = \sum_{i=1}^{2} w_{e,i} f_{e,i} \tag{17}$$

$$T_l = \sum_{j=1}^{2} w_{ph,j} f_{ph,j} \tag{18}$$

According to the Chapman–Enskog expansion, the relaxation times τ_e and τ_l can be obtained as follows [24]

$$\tau_e = 3a_e + \frac{1}{2} \tag{19}$$

$$\tau_l = 3a_l + \frac{1}{2} \tag{20}$$

The streaming step in the electrons is

$$f_{e,i}(x, t + \Delta t) = f^*_{e,i}(x - (-1)^i \Delta x, t + \Delta t) \tag{21}$$

To solve the phase change problem, a fixed grid approach is used in the phonons subsystem. The melting process takes place over a temperature range $T_m + \xi$ where ξ is a small quantity (typically 5 % of T_m [39]). The principle of the enthalpy method is to separate the sensible and latent heat components in the vicinity of the solid–liquid interface ($T_m - \xi < T_l < T_m + \xi$). The latent heat component is expressed in terms of the latent heat and liquid fraction, F_l, which is defined as:

$$F_l = \begin{cases} 1 & T_l > T_m + \xi \\ (T_l - T_m + \xi)/2\xi & T_m - \xi < T_l < T_m + \xi \\ 0 & T_l > T_m - \xi \end{cases} \tag{22}$$

Dynamically, the phase change zone is treated as a porous medium, see Fig. 2. The flow penetration into the medium depends on its permeability [39]. For the streaming step in the porous medium, if the node is totally solid, $f_{ph,j}$ is completely reflected. If the node contains a fraction of liquid $F_l \neq 1$, only a part of $f^*_{ph,j}$ is propagated, the other part is reflected and returned to the initial cell, i.e.,

$$\begin{aligned} f_{ph,j}(x, t + \Delta t) = {} & f^*_{ph,j}(x, t + \Delta t) \\ & + (1 - F_l)\left[f^*_{ph,j}(x - (-1)^j \Delta x, t + \Delta t) - f^*_{ph,j}(x, t + \Delta t) \right] \end{aligned} \tag{23}$$

3 Results and Discussion

The material of the film in the simulation was chosen as gold. And the thermal properties and optical parameters of TTM can be found in Ref. [13], unless otherwise

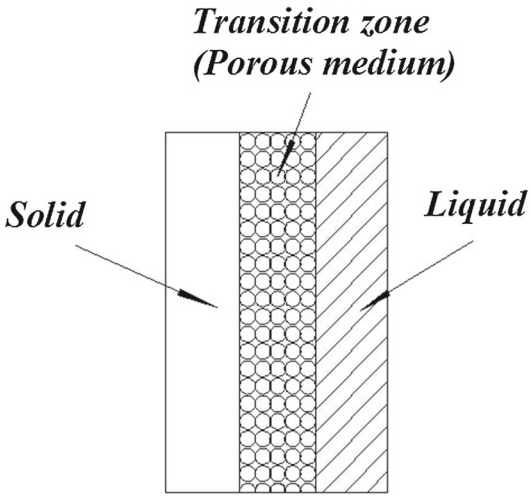

Fig. 2 Phase change

Table 1 Parameters of gold for LBM [38]

m_e	9.108×10^{-31} kg
N	5.9×10^{22} cm^{-3}
V_s	1900 m s^{-1}
T_F	6.4×10^4 K
$\omega_{e,0}$	2.03×10^{-17} s^{-1}
$\omega_{ph,0}$	1.27×10^{-16} s^{-1}

mentioned. And the parameters of LBM can be found in Table 1. To validate our computer code, the normalized electron temperature $\Theta_e = (T_e - T_{e,0})/(T_e - T_{e,0})\text{max}$ predicted by LBM and TTM is compared with the experimental data in Ref. [40]. The experiment measured the transient reflectivity changes, ΔR. Juhasz et al. [41] also showed that ΔR is proportional to ΔT_e near room temperature. Therefore, the normalized electron temperature changes can be deduced from the measured normalized reflectivity changes as $\Theta_e \approx (R - R_0)/(R - R_0)_{\max}$ [7]. Figure 3 shows the history of the normalized electron temperature Θ_e at the front surface and the rear surface predicted by the different numerical methods and the experimental data. The pulse width is 96 fs, the laser fluence J is 10 J·m^{-2}, and the length of the film L is 100 nm. It can be found that the results obtained by LBM are similar to those of TTM and both of them agree quite well with the experimental data.

For laser microstructuring with high precision, determination of the thermal damage zone size is of importance [8]. For that reason, the dependence of the melting threshold fluence on the thickness of gold films is also investigated. Figure 4 presents the comparison of the melting threshold fluences predicted by the LBM and the TTM and the experimental data in Ref. [42]. The melting threshold fluences are obtained numerically by adjusting the laser fluences J for which the maximum lattice temperature $T_{l,\max}$ just reaches the melting point (1336 K [13]). According to Fig. 4, the results predicted by the LBM coincide quite well with that of the TTM, while the

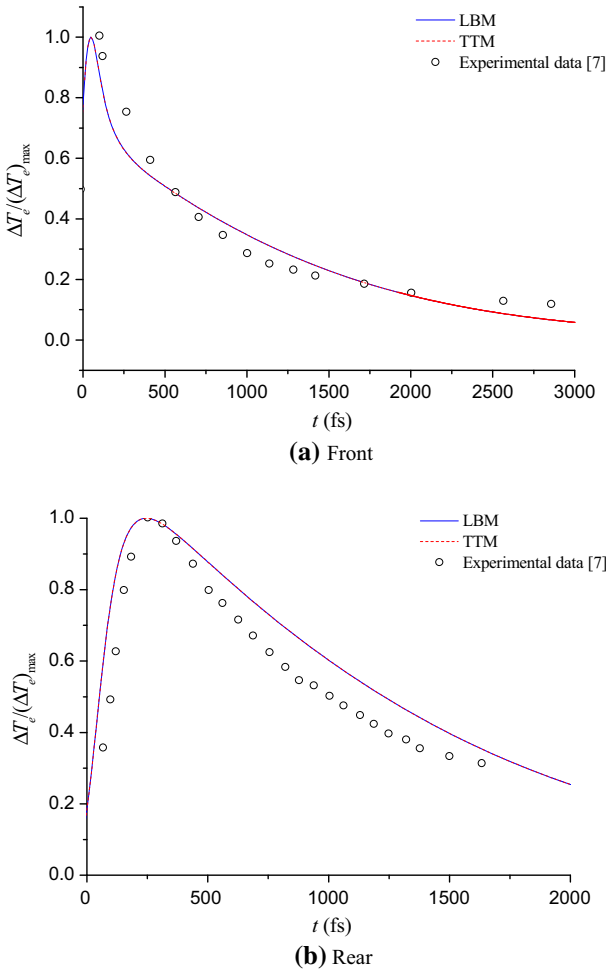

Fig. 3 Comparison between simulation results with different models and normalized electron temperature at the front and rear surface in Ref. [7] ($L = 100$ nm, $J = 10$ J·m^{-2}, $t_p = 96$ fs, $R = 0.93$ and $\delta_b = 0$)

experimental thresholds are a bit higher than our simulation results. Take the threshold of 300 nm film as an example. The experimental threshold is 0.59 J·m^{-2}, the result of the LBM is 0.51 J·m^{-2}, and TTM's result is 0.52 J·m^{-2}. That is mainly because our models do not include the effects of the electron drift velocity resulting from nonuniform electric temperature field [10]. However, the maximum difference between the experimental data and our simulation results (both LBM and TTM) is no more than 15 %.

In Figs. 3 and 4, it can be found that both the LBM and the TTM can catch the electron temperature and lattice temperature below the melting point quite well. However, when the phase change takes place, the TTM has to apply the interfacial tracking method which assumes the liquid area and the solid area are divided by an obvious interface [11, 13]. Figure 5 shows the lattice temperature distribution predicted by

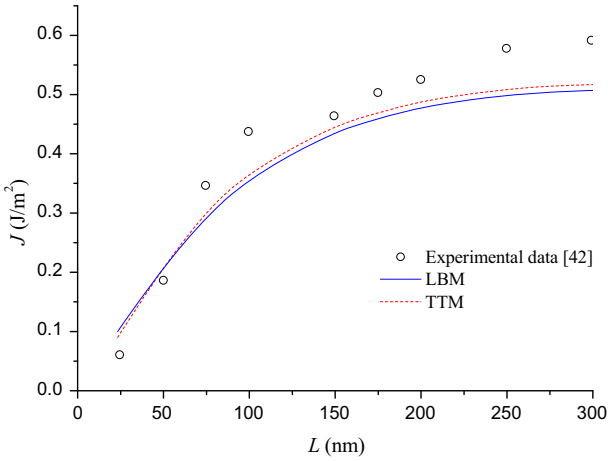

Fig. 4 Comparison between simulation results with different models and the melting threshold in Ref. [42] ($t_p = 600$ fs and $R = 0.926$ and $\delta_b = 0$)

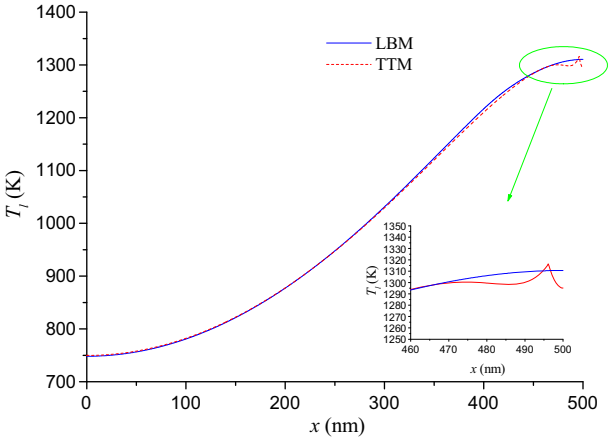

Fig. 5 Lattice temperature distribution for LBM and TTM ($L = 500$ nm, $J = 2500$ J·m^{-2}, $t_p = 20$ ps and $R = 0.6$)

different models at the moment of 200 ps for a 500 nm film irradiated by a 20 ps and 2500 J·m^{-2} laser. It can be seen that the lattice temperature predicted by the TTM experiences a sharp bulge at $x = 495$ nm. The local peak is just the location of the interface. The appearance of the bulge mainly derives from two reasons. Firstly, the lattice temperature at the interface has to be adjusted to accord with the nucleation dynamics equation [12]. Secondly, there is a mutation of the thermophysical properties at the two sides of interface, which is physically unwanted [11]. However, the lattice temperature predicted by the LBM is quite different. Since a transition area, which is treated as a porous medium, is added between the solid area and liquid area, the lattice temperature predicted by LBM can be smoothed at the interface (see the enlarged view of Fig. 5).

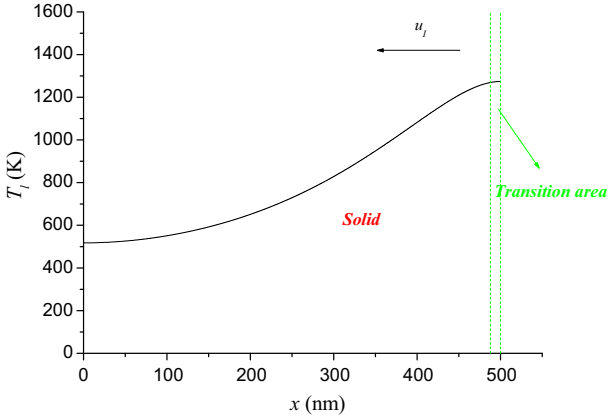

(a) $t = 10$ ps

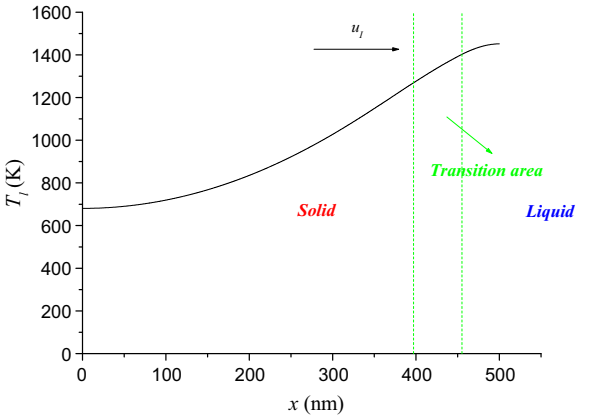

(b) $t = 100$ ps

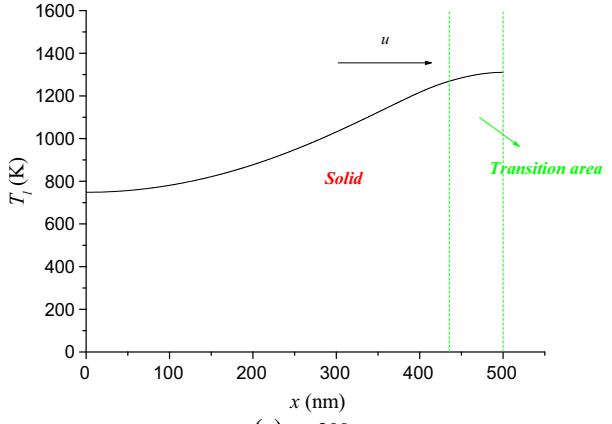

(c) $t = 200$ ps

Fig. 6 The movement of transition zone predicted by LBM ($L = 500$ nm, $J = 2500$ J·m^{-2}, $t_p = 20$ ps and $R = 0.6$)

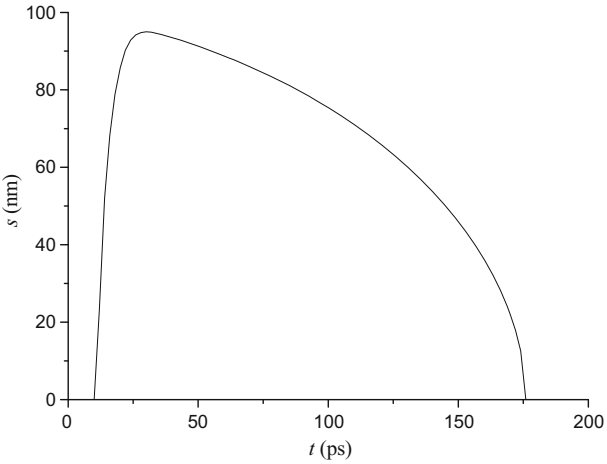

Fig. 7 The history of the melting depth s (L=500 nm, J=2500 J·m^{-2}, t_p =20 ps and R=0.6)

Figure 6 shows the movement of the transition area predicted by the LBM for a 500 nm film irradiated by a 20 ps and 2500 J·m^{-2} laser. Figure 6a reveals the melting behavior at the time of 10 ps when the melting process just takes place. It can be seen that at the beginning of the phase change, there is a transition phase, but no pure liquid, at the vicinity of the front surface. The transition area is going to the left, and length of the area Δl is 13.05 nm. At the moment of 100 ps when the melting process comes to the end and the resolidification happens, see Fig. 6b, the gold film can be divided into three parts, the solid area, the transition area and the liquid area. The length of the transition area Δl is 58.1 nm, and that of the liquid area is 44.85 nm. At 200 ps, see Fig. 6c, the liquid area disappears and the transition area, Δl, is 64.45 nm.

We define the melting core as the place, $x = x_m$, where the lattice temperature is just up to the melting temperature, i.e., $T_l(x_m) = T_m$. Numerically, the melting core is defined at the control volume that satisfies $|T_l\,[x(n_m)] - T_m|_{\min}$ where n_m is the node of the control volume which approximates the melting core, i.e., $x_m \approx x(n_m)$. Then, we set the melting depth as $s = L - x(n_m)$. Figure 7 displays the history of the melting depth s for the same parameters as Fig. 5. It can be seen that the melting process takes place at 12 ps since the melting curve starts at that point. And the melting depth s rises up to the peak, 95 nm, at 30 ps before it drops down to the zero at 174 ps. That is to say the resolidification happens at 30 ps and ends at 174 ps.

Figure 8 illustrates the history of the length of the transition area Δl for a 500 nm film suffering the irradiation of a 20 ps and 2500 J·m^{-2} laser. It can be found that the length of the transition area Δl rises up to 53.95 nm until t=12 ps. Then, it drops back to 35.6 nm at 24 ps. That is mainly because before 12 ps (the beginning of the melting process, see Fig. 7), there is no liquid phase and the transition area enlarges with the increasing lattice temperature. After that, the transition area turns into the liquid and the changing rate of liquid is more quickly than the growth rate of the transition area. After the moment of 24 ps, the length of transition area Δl shoots up to 95.65 nm at 128 ps. Then, the liquid phase vanishes and the transition area begins shrinking. At 248 ps, the transition area ends up.

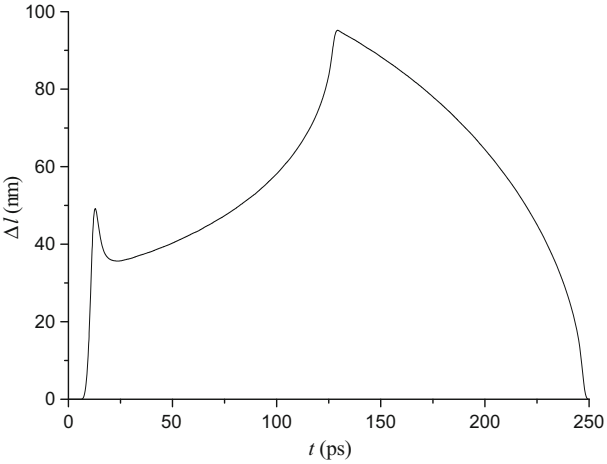

Fig. 8 The history of the length of the transition area Δl ($L = 500$ nm, $J = 2500\ \mathrm{J{\cdot}m^{-2}}$, $t_p = 20$ ps and $R = 0.6$)

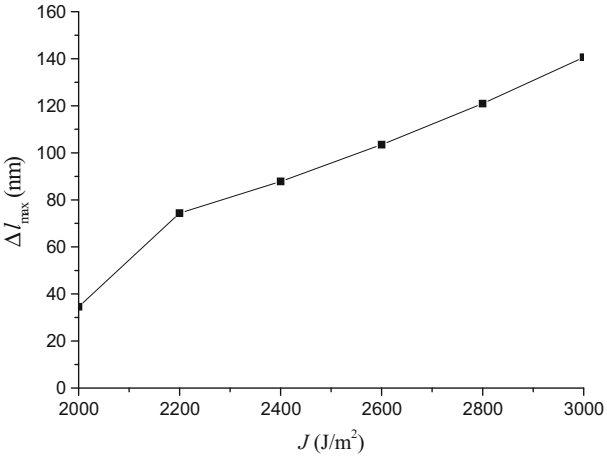

Fig. 9 J vs $\Delta l_{\max}$ ($L = 500$ nm and $t_p = 20$ ps)

Figure 9 shows the influence of the laser fluence J on the transition area. The pulse width t_p is set as 20 ps, and the length of the film L is 500 nm. According to Fig. 9, it can be seen that the maximum of Δl increases from 34.55 nm to 140.65 nm with the increasing fluences J, from 2000 $\mathrm{J{\cdot}m^{-2}}$ to 3000 $\mathrm{J{\cdot}m^{-2}}$. Figure 10 shows the influence of the pulse width t_p on the length of transition area. The laser fluence J is held at 2500 $\mathrm{J{\cdot}m^{-2}}$, and the length of the film L is 500 nm. It can be found that $\Delta l_{\max}$ fluctuates with the increasing pulse width t_p from 1 ps to 50 ps, but generally $\Delta l_{\max}$ of different pulse widths hovers at 95.5 nm. That is to say the influence of the pulse width on the transition area is not significant.

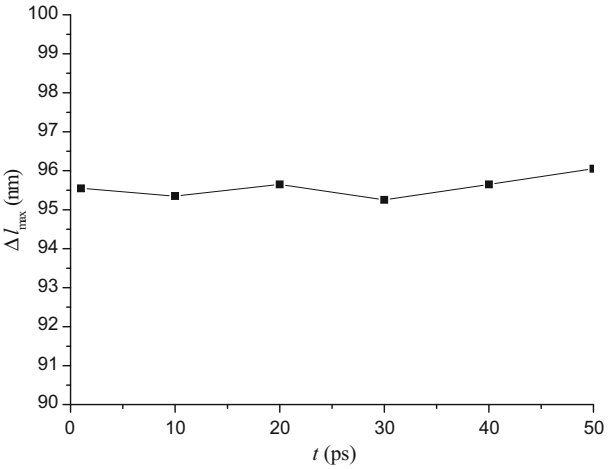

Fig. 10 t_p vs $\Delta l_{\max}$ ($L = 500$ nm and $J = 2500$ J·m^{-2})

4 Conclusions

The melting and resolidification of ultrashort laser interaction with thin gold film is investigated using LBM with the electron–phonon scattering term. A fixed grid approach is applied to describe the phase change, and the transition zone between solid and liquid is treated as the porous medium. Both the normalized electron temperature for 96 fs laser and the melting threshold for 600 fs laser predicted by the LBM agree with the experimental data quite well. Then, the melting behaviors predicted by both the TTM and the LBM of a 500 nm film irradiated by a 20 ps and 2500 J·m^{-2} laser are compared. The lattice temperature predicted by the TTM experiences a sharp bulge at the interface which is physically unwanted, while the interfacial temperature predicted by LBM is smooth. In addition, a melting core is defined as the place, $x = x_m$, where the lattice temperature is just up to the melting temperature, i.e., $T_l(x_m) = T_m$. The time-dependent width of the transition zone Δl is also investigated. It can be found that there are two peaks for the history of Δl, 53.95 nm at 12 ps and 95.65 nm at 128 ps. The influence of the laser fluence J and the pulse width t_p on the transition zone is also studied. It is found that when the pulse width t_p is set as 20 ps and the length of the film L is 500 nm, the maximum of Δl increases from 34.55 nm to 140.65 nm with the increasing fluences J, from 2000 J·m^{-2} to 3000 J·m^{-2}. When the laser fluence J is held at 2500 J·m^{-2} and the length of the film L is 500 nm, the influence of the pulse width on the transition area is not significant.

Acknowledgments The authors gratefully acknowledge the financial support from the Natural Science Foundation of China under Grant No. 51476102.

References

1. P. Hannaford, *Femtosecond Laser Spectroscopy* (Springer, Berlin, 2005)
2. D. Bourell, M. Wohlert, N. Harlan, S. Das, J. Beaman, Adv. Eng. Mater. **4**, 666 (2002)
3. W.N. Su, P. Erasenthiran, P.M. Dickens, P.I. Mech, Eng. C-J. Mec. **217**, 127 (2003)
4. J. Huang, Y. Zhang, J.K. Chen, Int. J. Heat Mass Transf. **52**, 3091 (2009)
5. A.K. Upadhyay, H.M. Urbassek, J. Phys. D Appl. Phys. **40**, 3518 (2007)
6. S.L. Anisimov, B.L. Kapeliovich, T.L. Perel' man, Sov. Phys. JETP **39**, 375 (1974)
7. T.Q. Qiu, C.L. Tien, ASME J. Heat Transf. **115**, 835 (1993)
8. J.K. Chen, J.E. Beraun, Numer. Heat Transf. A **40**, 1 (2001)
9. D.Y. Tzou, J. Heat Transf. **117**, 8 (1995)
10. J.K. Chen, D.Y. Tzou, J.E. Beraun, Int. J. Heat Mass Transf. **49**, 307 (2006)
11. I.H. Chowdhury, X. Xu, Numer. Heat Transf. A **44**, 219 (2003)
12. C. Konrad, Y.W. Zhang, Y. Shi, Int. J. Heat Mass Transf. **50**, 2236 (2007)
13. Y.W. Zhang, J.K. Chen, J. Appl. Phys. **104**, 054910 (2008)
14. Y.W. Zhang, J.K. Chen, ASME J. Heat Transf. **130**, 062401 (2008)
15. Y. Ren, J.K. Chen, Y. Zhang, Int. J. Heat Mass Transf. **55**, 1620 (2012)
16. J. Huang, Y. Zhang, J.K. Chen, Appl. Phys. A **95**, 643 (2009)
17. J. Huang, Y.W. Zhang, J.K. Chen, M. Yang, Front. Energy **6**, 1 (2012)
18. Y. Ren, C.W. Cheng, J.K. Chen, Y. Zhang, D.Y. Tzou, Int. J. Therm. Sci. **70**, 32 (2013)
19. Q. Peng, Y. Zhang, Y. He, Y. Mao, Int. J. Heat Mass Transf. **61**, 675 (2013)
20. L. Zhou, L. Li, Appl. Phys. A **116**, 2157 (2014)
21. Y. Yamashita, T. Yokomine, S. Ebara, A. Shimizu, Int. J. Thermophys. **27**, 627 (2006)
22. L. Yang, Y. Gan, Y. Zhang, J.K. Chen, Appl. Phys. A **106**, 725 (2012)
23. P. Ji, Y. Zhang, J. Phys. D Appl. Phys. **46**, 495108 (2013)
24. A.A. Mohamad, *Lattice Boltzmann Method, Fundamentals and Engineering Applications with Computer Codes* (Springer, London, 2011)
25. G. de Fabritiis, A. Mancini, D. Mansutti, S. Succi, Int. J. Mod. Phys. C Comput. Phys. Phys. Comput. **9**, 1405 (1998)
26. W. Miller, J. Cryst. Growth **230**, 263 (2001)
27. A.D. Brent, V.R. Voller, K.J. Reid, Numer. Heat Transf. **13**, 297 (1988)
28. W. Miller, S. Succi, D. Mansutti, Phys. Rev. Lett. **86**, 3578 (2001)
29. D. Chatterjee, S. Chakraborty, Phys. Lett. A **341**, 320 (2005)
30. D. Chatterjee, S. Chakraborty, Phys. Lett. A **351**, 359 (2006)
31. S.C. Mishra, N.C. Behera, A.K. Garg, A. Mishra, Int. J. Heat Mass Transf. **51**, 4447 (2008)
32. C. Körner, E. Attar, P. Heinl, J. Mater. Process. Technol. **211**, 978 (2011)
33. J. Zhao, P. Cheng, Int. J. Heat Mass Transf. **110**, 94 (2017)
34. S.I. Anisimov, Proc. SPIE **2793**, 192 (1997)
35. P.B. Allen, Phys. Rev. Lett. **59**, 1460 (1987)
36. J.M. Ziman, *Electrons and Phonons* (Oxford Univ. Press, London, 1960)
37. M.I. Kaganov, I.M. Lifshitz, L.V. Tanatarov, Sov. Phys. JETP **4**, 173 (1957)
38. J.K. Chen, W.P. Latham, J.E. Beraun, J. Laser Appl. **17**, 63 (2005)
39. E.A. Semma, M.E. Ganaoui, R. Bennacer, C. R. Mecanique **335**, 295 (2007)
40. S.D. Brorson, J.G. Fujimoto, E.P. Ippen, Phys. Rev. Lett. **59**, 1962 (1987)
41. T. Juhasz, H.E. Elsayed-Ali, X.H. Hu, W.E. Bron, Phys. Rev. B **45**, 13819 (1992)
42. B.C. Stuart, M.D. Feit, S. Herman, A.M. Rubenchik, B.W. Shore, M.D. Perry, J. Opt. Soc. Am. B **13**, 459 (1996)